J. Micromech. Microeng. **18** (2008) 065015 (13pp) doi:10.1088/0960-1317/18/6/065015

The lateral migration of neutrally-buoyant spheres transported through square microchannels

Young Won Kim and Jung Yul Yoo

School of Mechanical and Aerospace Engineering, Seoul National University, Seoul 151-744, Korea

E-mail: jyyoo@snu.ac.kr

Received 25 February 2008, in final form 3 April 2008
Published 6 May 2008
Online at stacks.iop.org/JMM/18/065015

Abstract
The lateral migration of neutrally-buoyant particles transported through square microchannels has been experimentally investigated over a Reynolds number range of $0.06 \leqslant Re \leqslant 58.65$ at the ratio of channel hydraulic diameter to particle size, $\lambda \approx 14$. Flow Reynolds numbers are determined by applying a conventional particle-tracking algorithm to small tracer particles, while novel imaging techniques have been proposed for identifying and defining the measurement depth of large test particles. By analyzing the spatial distributions of spherical particles, it is revealed that lateral migration of particles markedly occurs even at very low Re, which is induced by the high shear rate due to the small-scale effect. The particle equilibrium position is obtained as a function of Re, and the critical Re at which the particle equilibrium position starts to increase is found in the range $20 \leqslant Re \leqslant 30$. The outermost edge of the particle cluster is also in good agreement with previously available data, which provides a good quantitative basis for designing microfluidic devices that are to be used for plasma separation from whole blood.

Nomenclature

A	magnitude of scaled force
D	test particle diameter
d	tracer particle diameter
D_h	channel hydraulic diameter
D_t	circular capillary diameter
$f(y)$	probability density function
g	gravitational acceleration
H	channel width
I	image intensity
$I_{m,n}$	image intensity of the pixel element containing (x_m, y_n)
k	sequence of particle image frame
L	measurement station from the inlet of test channels
L_3	reduced tube length
L_e	entry length
M	magnification of objective lens
n	refractive index
NA	numerical aperture
p	pressure on a particle surface
R	tube radius
r	radial distance
Re	Reynolds number
U	mean fluid velocity
u	streamwise velocity component
$U_{\max}$	maximum fluid velocity at the channel center
U_{TS}	terminal settling velocity of a particle
y_e	particle equilibrium position
y_o	outermost edge of particle cluster
z	distance from focal plane
(x, y)	local Cartesian coordinates
β	mean image-intensity gradient
Δx	width of a pixel
δ_{zm}	measurement depth
$\dot{\gamma}_w$	wall shear rate
$\epsilon_{()}$	experimental errors in y_e and y_o
λ	ratio of channel hydraulic diameter to particle diameter, D_h/D
λ_0	wavelength of the light in vacuum
μ_m	dynamic viscosity of water–glycerol mixture
μ_w	dynamic viscosity of water
ν	kinematic viscosity
ρ_m	density of water–glycerol mixture

ρ_p particle density
ρ_w water density
θ collection angle

1. Introduction

Microfluidics has attracted considerable attention for the past few decades because of its wide scientific and engineering applications in industries including life science and combinatorial synthesis [1]. Some of the most excellent and enlightening overviews on microfluidics can be found in Stone and Kim [1] and Gravesen *et al* [2].

Normally, the length scale of microchannels is in the order of up to several hundred microns and that of particles being transported is in the order of less than 10 μm. This leads to the situation of solid–liquid two-phase flows because the ratio of the channel size to the particle size is relatively large and the channel Reynolds number (*Re*) is small but finite in microchannels [1]. Under such flow conditions, a particle will not necessarily follow fluid streamlines, so lateral migration is frequently observed [3, 4]. This lateral migration can be utilized for separating biological particles [5, 6] or focusing of DNAs [7] in capillary-based microchannels with dilute suspension flows.

The earliest observation of lateral migration of macromolecules can be traced back to Poiseuille [8] who worked on blood flow in a capillary, where the red blood cells (RBCs) migrate away from the wall and are concentrated around the center. This phenomenon is called Fahræus–Lindqvist effect that causes the flow resistance to decrease inside the capillary [9]. Uijttewaal *et al* [10] showed spatial distributions of spherical particles as well as RBCs undergoing lateral migration in a rectangular glass capillary with a width of 100 μm. More recently, Eloot *et al* [11] have investigated radial migration of neutrally-buoyant particles in circular capillaries with diameters $D_t = 210$ and 530 μm by considering different surface conditions inside the capillaries. Rather than studies which are more focused on the lateral migration, Xuan and Li [12] studied particle motions in converging-diverging channels. Staben and Davis [13] and Staben *et al* [14] studied relative motions between the fluid and the particle experimentally [13] and numerically [14], respectively. In any event, fundamental studies on the particle migration in such microscale flows lag behind those carried out widely in macroscale flows, not to speak of the extensive investigations on the single-phase microscale flows from the point of view of classical fluid mechanics [15–18].

In retrospect, lateral migration of solid particles in dilute suspensions has been extensively and systematically investigated in macroscale duct flows since Segré and Silberberg [3] observed that the neutrally-buoyant particles accumulate at certain equilibrium positions in a tube. This work triggered a series of experimental and theoretical studies regarding tube flow [19, 20], channel flow [21] and Couette flow [22], laden with neutrally-buoyant particles [4, 19, 23] and non-neutrally-buoyant particles [21, 24]. Ho and Leal [25] showed by a regular perturbation method at low *Re* that the equilibrium position (r/R) is 0.6, which is in agreement with the experimental data of Segré and Silberberg. Schonberg and Hinch [26] lifted this low-Reynolds-number restriction by using matched asymptotic expansion method and presented the particle equilibrium position up to $Re = 150$. In general, as *Re* increases, equilibrium position shifts toward the wall [3, 26, 27] and may appear with multiple-equilibrium positions [27, 28]. Moreover, direct numerical simulation has been used for extensively examining single particle motion under radial migration [29] and for characterizing the effect of particle volume fraction with many particles [30]. Other than Poiseuille flows in circular pipes or in planar channels, Chun and Ladd [31] have investigated inertial migration of neutrally-buoyant particles in a square duct, which shows that there exist eight and four stable equilibrium positions at $Re = 100$ and 500, respectively. Interesting observations reported in macroscale flows in the case of experimental works are the spatial distribution of particles, the particle equilibrium position and the outermost edge of particle cluster. The first two observations are closely related to particle separation techniques in a capillary [5, 6] while the third one, traditionally considered to be less important than the others, is becoming important for improving plasma selectivity from the whole blood in microfluidic devices [32–34].

However, little is known about the characteristics of lateral migration in microscale flows even in a square channel so far. In fact, in designing a viable separation process, it will be necessary to optimize both the channel design and operation conditions of the devices to maximize the recovery of the desired species and to minimize the processing time [5]. In this sense, the present study is crucially important for providing design rules of the microfluidic devices for unit operations, such as separations and concentrations. In fact, the features of lateral migration of neutrally-buoyant particles in a square channel are known to be different from those in a circular channel or a planar channel [31]. Specifically, the particle equilibrium position in a square channel is farther than that in a circular channel or planar channel, according to the previous numerical simulation [31]. Further, particles are gathered at each corner in a square duct flow at high Reynolds numbers, which is not observed in a circular or planar channel flow [31]. In addition, the shear rate in microchannel flows is much higher than that in macroscale flows due to the scale effect at a given *Re*. In this circumstance, it is expected that high shear rate in microchannel flows possibly induces strong particle migration [29, 35]. Nevertheless, the lateral migration in square channels, not to speak of square microchannels, still remains far from fully understood.

Thus, the objective of the present study is to give a more systematic explanation on the characteristics of the particle-laden microscale flows in square microchannels. More specifically, this work investigates experimentally the lateral migration of neutrally-buoyant particles in the range of $Re \leqslant 58.65$ with the ratio of channel hydraulic diameter to particle size, $\lambda \approx 14$. In section 2, we describe measurement techniques in detail. A novel measurement technique is proposed, in which the fluid velocity is obtained from the small tracer particles by applying the conventional particle-tracking algorithm while the large test particles are identified

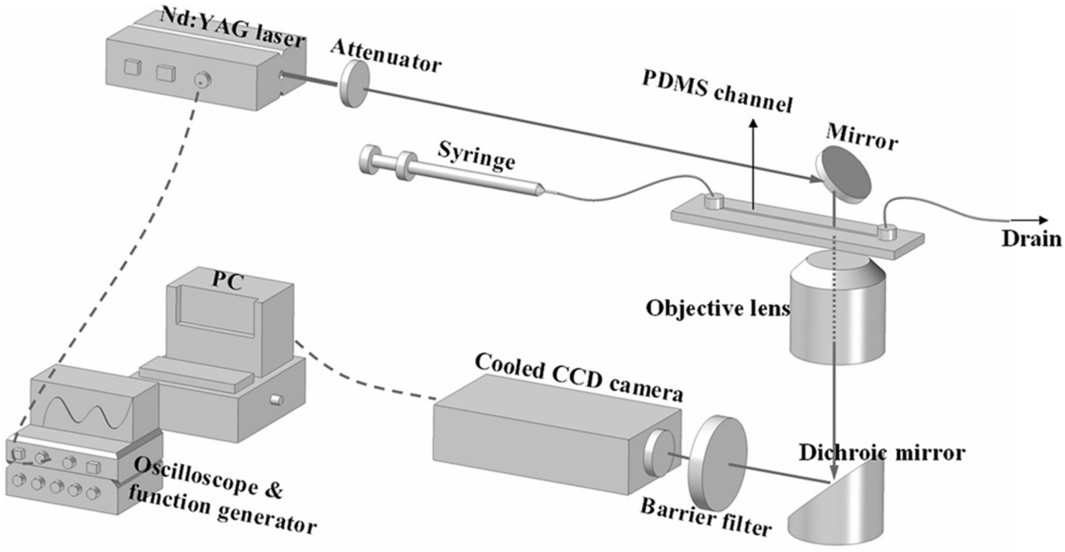

Figure 1. The experimental setup consists of an epi-fluorescent microscope, a cooled-CCD camera and a double-pulsed Nd:YAG laser. Fluorescently labeled polystyrene particles of different sizes with a peak excitation wavelength of 540 nm and a peak emission wavelength of 570 nm are used. The laser produces green light with a wavelength of 532 nm and pulse duration of 4–6 ns, which sufficiently freezes the motion of the particle without making streaks. Initially, the power of the laser is reduced through the beam attenuator, before the beam is directed via a mirror onto the upper side of the water chamber where the circular microchannel is placed. Red light with a wavelength of 570 nm emitted from the fluorescent particles, which has been excited by the green light with a wavelength of 532 nm from the laser beam, is focused by the objective lens and introduced into the CCD camera.

and their measurement depths are calibrated by utilizing a newly proposed definition of the image-intensity gradient. In section 3, as our primary results, particle distributions at various *Re* will be presented and compared with the previous studies, in terms of the entrance effect and the shear rate. Equilibrium position and the critical *Re* at which it starts to increase are compared with asymptotic theory [26]. Further, the outermost edge of particle cluster is demonstrated with reduced tube length [3]. Finally, we conclude our study in section 4.

2. Experiments

2.1. Experimental apparatus and conditions

The experimental setup of the present study as shown in figure 1 consists of a double-pulsed Nd:YAG laser (SLI-PIV, Continuum Electro-Optics, USA), an epi-fluorescent microscope (IX50, Olympus, Japan) and a cooled-CCD camera (SensiCam, PCO, Germany), which is quite typical of a standard micro-PIV/PTV system described elsewhere [36]. The laser used produces green light with a wavelength of 532 nm and a laser pulse duration of 4–6 ns, which sufficiently freezes the motion of the particle without making particle streaks. Fluorescently labeled microspheres in the flow field absorb the green light and emit the red light with an emission peak of about 570 nm. The emitted light passes through the cooled-CCD camera via barrier filter, where the scattered light from the green light is filtered out and the red fluorescence from the particle is recorded.

Experimental conditions are summarized in table 1. The particle volume fraction is sufficiently low, so that the particle-to-particle interaction can be neglected [27]. According to the channel hydraulic diameter D_h, different magnifications of the objective lens are used. Measurements are made at a fixed location downstream of the inlet of each channel, i.e., at $L/D_h = 400$, where L is the distance from the inlet to the measurement station, at various flow conditions as summarized in table 2.

Table 1. Summary of experimental conditions.

	Channel hydraulic diameter[a], $D_h (\mu m)$	
	87.5	140.9
Particle size		
Test particle, D (μm)	6	10
Tracer particle, d (μm)	2	2
$\lambda = D_h/D$	14.5	14.1
Re	0.12–14.95	0.06–58.65
Particle volume fraction (%)		
Test particle	0.1	0.1
Tracer particle	0.001	0.001
Objective lens		
Magnification	40×	10×
Numerical aperture (NA)	0.75	0.35
Measurement station, L/D_h	400	400

[a] The channel hydraulic diameter is defined by $D_h = \frac{4\mathscr{A}}{\mathscr{P}}$, where $\mathscr{A}$ is the cross-sectional area of the channel and $\mathscr{P}$ is the wetted perimeter.

2.2. Materials

Fluorescent particles (Duke Scientific, USA) of different sizes are used in the present experiment. Small fluorescent particles with a diameter of $d = 2 \pm 0.1$ μm are adopted as tracers,

Table 2. Summary of fluid velocities and the corresponding *Re* for two channel sizes, at which observations are made in the present study.

$D_h = 87.5\ \mu$m		$D_h = 140.9\ \mu$m			
U_{max} (cm s^{-1})	*Re*	U_{max} (cm s^{-1})	*Re*	U_{max} (cm s^{-1})	*Re*
0.44 ± 0.01	0.12 ± 0.01	0.14 ± 0.02	0.06 ± 0.01	46.01 ± 0.79	21.49 ± 1.08
2.40 ± 0.03	0.69 ± 0.03	0.26 ± 0.01	0.12 ± 0.01	51.95 ± 1.40	24.27 ± 1.46
6.18 ± 0.08	1.79 ± 0.08	0.70 ± 0.02	0.32 ± 0.02	52.51 ± 1.16	24.53 ± 1.35
8.25 ± 0.14	2.39 ± 0.12	1.06 ± 0.03	0.94 ± 0.03	54.45 ± 1.47	25.44 ± 1.53
10.23 ± 0.24	2.97 ± 0.16	1.42 ± 0.03	0.66 ± 0.03	58.24 ± 0.73	27.20 ± 1.25
10.36 ± 0.29	3.00 ± 0.18	2.37 ± 0.04	1.11 ± 0.05	75.20 ± 1.07	35.12 ± 1.67
14.30 ± 0.52	4.15 ± 0.29	3.23 ± 0.05	1.51 ± 0.07	75.70 ± 1.75	35.36 ± 1.99
14.39 ± 0.39	4.17 ± 0.25	3.25 ± 0.04	1.51 ± 0.06	80.52 ± 1.05	37.60 ± 1.74
16.23 ± 0.35	4.71 ± 0.25	5.21 ± 0.08	2.43 ± 0.12	80.55 ± 1.82	37.63 ± 2.10
20.53 ± 0.49	5.95 ± 0.34	6.62 ± 0.12	3.09 ± 0.16	81.14 ± 2.21	37.91 ± 2.29
20.92 ± 0.75	6.07 ± 0.42	7.94 ± 0.18	3.71 ± 0.21	93.18 ± 1.40	43.52 ± 2.10
28.53 ± 0.75	8.27 ± 0.49	18.90 ± 0.13	8.82 ± 0.35	96.60 ± 1.25	45.11 ± 2.09
28.60 ± 1.07	8.30 ± 0.58	19.29 ± 0.53	9.01 ± 0.55	103.31 ± 1.59	48.25 ± 2.35
35.32 ± 1.01	10.25 ± 0.63	31.40 ± 1.35	14.68 ± 1.12	112.26 ± 2.16	52.44 ± 2.76
35.57 ± 0.60	10.31 ± 0.52	37.78 ± 0.96	17.65 ± 1.03	116.07 ± 1.55	54.21 ± 2.53
51.55 ± 0.60	14.95 ± 0.67	39.32 ± 0.86	18.37 ± 1.01	125.55 ± 2.32	58.65 ± 3.03

and large particles with diameters of $D = 6 \pm 0.9\ \mu$m and $10 \pm 1.2\ \mu$m are chosen as our test particles of interest. Large particles with $D = 6 \pm 0.9\ \mu$m are for the case of $D_h = 87.5\ \mu$m, while those with $D = 10 \pm 1.2\ \mu$m are for the case of $D_h = 140.9\ \mu$m, as summarized in table 1. The density of the particles used here is about 1.05 g cm^{-3}, which is slightly larger than that of water. Therefore, a particle released in still water reaches a terminal settling velocity [37] defined as

$$U_{TS} = \frac{D^2(\rho_p - \rho_w)g}{18\mu_w}. \qquad (1)$$

From equation (1), we obtain $U_{TS} = 0.98\ \mu$m s^{-1} and 2.7 μm s^{-1} for particles with $D = 6\ \mu$m and 10 μm, respectively. In fact, it was observed that these particles settle down on the bottom of the channel wall in several minutes due to the density difference from the fluid. Therefore, the density of the test fluid was matched to that of the particle by mixing glycerol with water in the volume ratio of 2.2:7.8. At this condition, it is known that the dynamic viscosity of the water–glycerol mixture is 0.014–0.015 g cm^{-1} s^{-1} at room temperature [27]. Then, it was observed that the particles neither settle down nor float around for 24 h at room temperature.

2.3. Fabrication of the PDMS microchannels and tubing

As test channels, two square PDMS microchannels of different sizes were fabricated using soft lithography process [38]. In the present study, both the film mask printed from high-resolution printer as a photomask to generate a master in UV photolithography and the master as a mold structure were provided from commercial services. To increase the uniformity of the height of photoresist, we used a 6″ Si wafer rather than a 4″ Si wafer, on which the SU-8 (MicroChem, USA) is coated with desired height. To produce replicas, PDMS (Dow Corning, USA) and curing agent were mixed in the volume ratio of 10:1 and stirred vigorously. The mixture was degassed in a desiccator, cast onto the master and then cured in an oven at 85° C for 10 h. A portion of the PDMS mold within the channel design was cut and peeled off from the master. Holes were punched at both ends of the channel to allow tubing. To create a highly sealed channel, the PDMS replica and 500 μm thick glass were bonded after oxidizing the surface of both the PDMS channel and the glass by oxygen plasma treatment. Also, we confirmed that the PDMS channels are substantially straight.

The resultant dimensions of the bottom width and the height of each channel are 87 × 88 μm and 138 × 144 μm. The channel height corresponds to the height of the patterned SU-8 on each wafer, which was measured by a profiler (150M, VEECO, USA). To confirm the squareness of the channel cross-section, we measured the widths of the top and bottom walls of each test channel, which are 88 ± 1.32 μm and 87 ± 1.32 μm for the small channel, and 139 ± 1.32 μm and 138 ± 1.32 μm for the large channel. Hence, we assume that the cross-sections of both test channels are sufficiently square. The calculation of the channel hydraulic diameter is based on the bottom width and the height of the channel.

The downstream end of a 15 cm long Teflon tube (ID ∼ 750 μm, OD ∼ 1.6 mm) is glued with the inlet hole of the PDMS channel, and the upstream end of this capillary is connected with a syringe via a luer-lock connector (Upchurch Scientific, USA). The outlet hole of the PDMS channel is glued with a silicone tube (ID ∼1 mm) for drain as shown in figure 1. In this case, there occurs no lateral migration in the Teflon tubing, because the tube diameter is substantially large relative to the particle size [27], while there is sufficient mixing due to the inlet reservoir of which the inner diameter is 3 mm and the height is 3 mm.

2.4. Experimental procedures

Dried particles which will serve as large test particles would not be mixed well with the water–glycerol mixture without some surface treatment. Therefore, as a surface-active agent, 100 μl of isopropyl alcohol (Sigma Aldrich, USA) is added from a micropipette into a cleaned glass bottle that contains a small amount of dried fluorescent particles. Then, the water–glycerol mixture is added into the bottle until the particle volume fraction reached about 0.1%. On the other hand, as tracer particles a small amount of 2 μm size particles provided by the manufacturer in the form of a suspension with a particle volume fraction of 1% is added into the bottle containing the large test particles suspended in the water–glycerol mixture, until the volume fraction of the tracer particles reaches about 0.001%. Now, the bottle containing both the tracer particles and the test particles suspended in the water–glycerol mixture is put into the ultrasonic cleaner (2510, Branson, USA), which is set to be in operation for 20 min to prevent the particle-to-particle aggregation. Then, a disposable plastic syringe is filled with the suspensions without any trapped air bubbles. The volume of the syringe is 1 ml for the test channel with $D_h = 87.5$ μm and 5 ml for that with $D_h = 140.9$ μm. Syringe plunger is depressed manually until the downstream end of silicone tube which is open in the atmosphere becomes filled with the solution. The syringe is then placed on syringe holder of the syringe driver (210, KD Science, USA).

No flow fluctuations were observed in the syringe pump (minimum linear travel rate of 0.57 μm h^{-1}) even at lowest velocities (typically larger than the order of several mm s^{-1} for both test channels). The objective lens of the microscope is focused on the midplane between the top and bottom walls of the test channel, which was realized by reading the scale of the fine-focusing knob of the microscope at the top and bottom walls of the test channel. This procedure is typically used in most experiments involving microscopic observation [39]. The fine-focusing knob of the microscope used here has 1 μm resolution along the vertical direction, parallel to the optical axis.

2.5. Imaging

A cooled-CCD camera with a 1300 × 1024 pixel array and 12 bit resolution is connected to the image-grabbing board (PCO PCI interface board 520/525) mounted on a personal computer. Four hundred pairs of particle image frames are obtained at a rate of 5 Hz at a given flow condition, which are needed to perform two-frame particle-tracking velocimetry to obtain fluid velocities using tracer particles. In order for the flow to reach the desired speed, there was a time gap between the start of the syringe pump and the instant when we started to collect images. Camera software (CamWare, PCO, Germany) utilized in the present study grabs a pair of image frames in the file format as '*k*A.tif' and '*k*B.tif', where *k* is the sequence of the image frames. The time interval between the two images of a pair depends on the Reynolds number. It ranges from several milliseconds for the lowest *Re* to several tens of microseconds for the highest *Re*, so that the particle displacement between the two images of a pair grabbed near the center of the channel is about 10–15 pixels. Prior to capturing particle images, a manual calculation was made to cross-check algorithm correctness using several pairs of images. For test particles, every first frame, i.e. '*k*A.tif' only, was used for our data analysis. Image frames were captured with 2 × 2 binning mode to increase the signal-to-noise ratio, so that 1 pixel of an image frame corresponds to 1.28 × 1.28 μm and 0.32 × 0.32 μm, respectively, for $M = 10$ and 40.

2.6. Measurements of fluid velocities

We adopted 2 μm diameter particles as tracer particles ($D_h/d \approx 44$ and 70 for $D_h = 87.5$ μm and 140.9 μm, respectively) since they are small enough compared to the channel size for the lateral migration to hardly occur, as also delineated in Matas *et al* ($D_t/D = 43$) [27]. In other words, the size of the tracer particles in the present study is beyond the range of particle-size ratio for the lateral migration to occur. As speculated, there was no depletion of these tracer particles near the centerline of the microchannels when we seeded only the smaller particles in the flow. More importantly, the same is true when we seeded both the tracer particles and the test particles in the flow. This size of small tracer particles helps obtain the fluid velocity vector field over the whole channel width to define the velocity profile needed for calculating *Re*.

To investigate the particle behavior at a specific *Re*, we use the suspensions where the small tracer particles of $d = 2$ μm are mixed with large test particles of $D = 6$ μm or 10 μm for dual-purpose measurements, i.e., determinations of the background flow *Re* with small tracer particles and the particle motion with large test particles of our interest. Thus, it is necessary to separate the images of the tracer particles from those of the test particles because large particles may not necessarily follow the fluid streamlines, which may cause errors in the estimation of the flow *Re*. Accordingly, we first consider a frame of particle images where both the tracer particles ($d = 2$ μm) and the test particles ($D = 10$ μm) are present as shown in figure 2(*a*). From the original frame of particle images (figure 2(*a*)), the separation of the particle images in accordance with the particle size can be achieved by performing a series of morphological operations, which is detailed in the caption of figure 2.

To calculate the fluid velocity from tracer particle images, the bright particles are identified by giving a reasonable threshold in the particle intensity [40]. Particle center with sub-pixel resolution is determined by fitting a two-dimensional Gaussian function to the intensity profiles of the particle image using our in-house code [40]. To estimate $Re = \rho_m U D_h/\mu_m$, U should be known. Figure 3 gives an outline of how the mean fluid velocity is determined. We obtain a velocity profile (figure 3(*c*)) from the vector field (figure 3(*b*)) by line-by-line averaging along the streamwise direction, while the vector field (figure 3(*b*)) can be obtained from the raw vectors (figure 3(*a*)) by spatially averaging at specified grid points, where the grid lines are not shown for clarity. Actually, these raw vectors are the direct results of the particle-tracking algorithm applied to 400 pairs of image frames. Once the maximum velocity $U_{\max}$ is specified, the mean fluid velocity is calculated using the approximation given by Purday [41] (see the caption of figure 3), which gives the relation between $U_{\max}$ and U for a given channel aspect ratio. Accordingly, we have $U_{\max} = 2.115U$ for $D_h = 87.5$ μm and $U_{\max} = 2.113U$ for $D_h = 140.9$ μm. The number of grid points is 50 in the lateral direction, so that the spatial resolution is $D_h/50$ laterally.

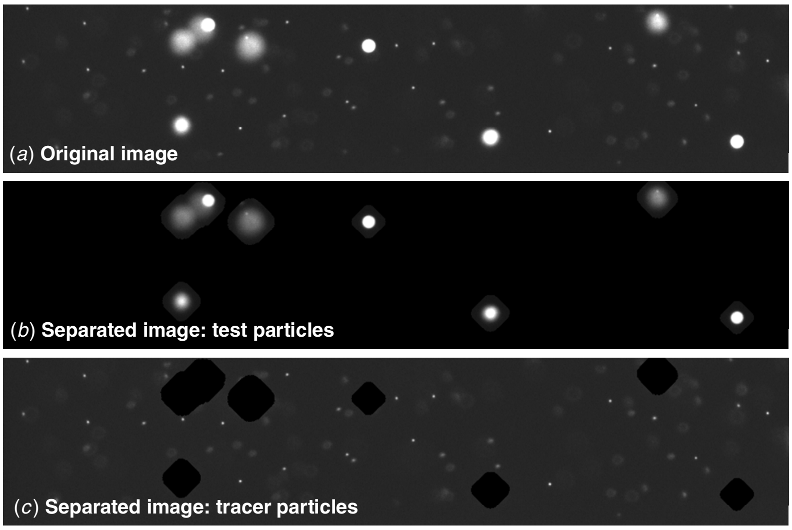

Figure 2. Particle image separation according to the particle size was successfully achieved by the following digital image processing. (1) The original image frame (*a*) was converted to the form of a binary image, in such a manner that a pixel element is assigned the value of either '1' or '0' by contrasting its intensity with a reasonable threshold intensity, where '1' and '0' correspond to the intensity of particles (both tracer particles and test particles) and background, respectively. (2) By performing image erosion involving several iteration processes, we eliminated small tracer particle images ($d = 2$ μm) from the image frame obtained in step (1), while the sizes of the large test particles can be reduced depending on the number of iterations during this image erosion. (3) Then, we performed an image dilation process for the image frame obtained in step (2), in order to recover the original particle size of the large particle with $D = 6$ μm or 10 μm. (4) We performed pixel-by-pixel multiplication of the particle image obtained in step (3) with the original particle image to obtain particle image frame (*b*). (5) Then, pixel elements corresponding to the value of '0' from the image frame obtained in step (3) were set to be '1', while those corresponding to the non-zero value were set to be '0'. Finally, these values were multiplied to the original image frame (*a*) by pixel-by-pixel to obtain particle image frame (*c*).

In this manner, maximum velocities and the corresponding Reynolds numbers at which lateral migration will be investigated are summarized in table 2 according to D_h. The error associated with *Re* comes from the following experimental errors: (1) random error due to the measurement of the fluid velocity, (2) error caused by uncertainty in the measurement of dynamic viscosity [27] and (3) pixel reading error in determining the channel walls in the particle image frame. The pixel reading errors are ± 2 pixels and ± 1 pixel for $D_h = 87.5$ and 140.9 μm, respectively.

2.7. Identification of large particles

To determine concentration distributions of test particles, image frames involving only large particles, which are obtained as explained in the previous subsection, are analyzed. However, in an image frame, one can observe both in-focus particles and out-of-focus particles because volume illumination [42, 43] is used for the present microscale flows. In this case, the particles having an intensity below a certain threshold level can be eliminated for better depth-of-field resolution, since usually an out-of-focus particle has lower intensity than that of an in-focus particle. However, we observe that a particle with a well-defined outline, deemed to be an in-focus particle, has a lower intensity than a brighter particle with a blurred outline, regarded as an out-of-focus particle. This means that the particle intensity itself may not be appropriate as a criterion for identifying the large test particles. We consider that this ambiguity can be caused by the small but non-negligible polydispersity in the particle-size distribution of test particles and the variation of laser power with time. Thus, we only take the particles with well-defined outlines as in-focus particles. There may be some concerns that two attached particles or two particles lying on top of each other can be observed in the flow field. However, according to our manual check, these aggregated particles occupy approximately 0.4% of all the particles qualified for our input data. Thus, in the statistical sense, we believe that these aggregated particles hardly affect our main results at such a very low particle volume fraction of 0.1%.

To select particles with well-defined outlines, we first introduce the 'image-intensity gradient' of the particle image. To aid an understanding of how we define this image-intensity gradient, we consider the illustration in figure 4(*a*), where grids and the large circle indicate the pixel elements and outline of the test particle in the image frame. The image-intensity gradient at a certain point (x_i, y_j) in the particle image is defined by the first-order difference scheme as follows:

$$\left.\frac{\partial I(x,y)}{\partial x}\right|_{(x_i,y_j)} = \frac{\frac{1}{6}\left(\sum_{m=i-2}^{i-1}\sum_{n=j-1}^{j+1} I_{m,n} - \sum_{m=i+1}^{i+2}\sum_{n=j-1}^{j+1} I_{m,n}\right)}{3\Delta x}. \qquad (2)$$

In practice, the pivot pixel element of our calculation contains the particle center, as represented by (x_i, y_j) in figure 4(*a*). The particle center is found by 2D Gaussian curve fitting in the same way as adopted for the tracer particles previously. We next obtain averaged intensities of 6 pixels as outlined

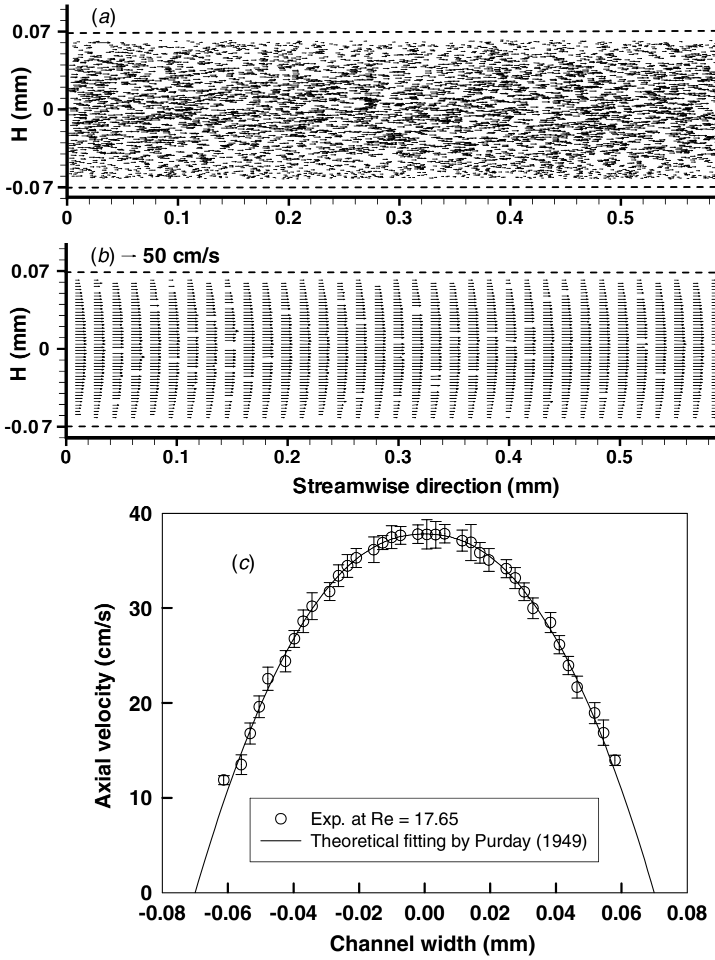

Figure 3. Particle-tracking results obtained from the tracer particles of $d = 2\ \mu$m, measured at $L/D_h = 400$: (*a*) instantaneous velocity vectors, (*b*) spatially-averaged velocity vectors at specified grid points with the grid lines not shown but the dotted lines indicating the channel walls and (*c*) the velocity profile obtained from (*b*) by taking line-by-line averaging along the streamwise direction, where error bars denote standard deviation from the mean. Actually, this figure is obtained at $U_{\max} = 37.78 \pm 0.96$ cm s^{-1} for $D_h = 140.9\ \mu$m, which is one of the flow conditions considered in the present study as shown in table 2. The solid line in (*c*) is the curve fitting using the approximation given by Purday [41], where $u(y) = U_{\max}[1 - (y/H)^q]$ with $q = 2 + 0.3(\alpha - 1/3) \approx 2.2$ and $\alpha = 1.04$ is the actual channel aspect ratio for $D_h = 140.9\ \mu$m in the present study.

with dashed rectangles adjacent to the particle center. Then, intensity gradient at (x_i, y_j) can be calculated by using these averaged intensities on the basis of equation (2), where $3\Delta x$ indicates the distance between both centroids of the dashed rectangles. The calculation of image-intensity gradient is repeated at the next pixel element represented by (x_{i+1}, y_j), (x_{i+2}, y_j) and so forth. Since our calculation is carried out radially from the particle center, the second index j is fixed.

In figure 4(*b*), the image-intensity gradient $\partial I(x, y)/\partial x$ is plotted against pixel distance from the particle center for both the particle with well-defined outline (particle A) and the particle with blurred outline (particle B), where '1' on the abscissa denotes the particle center. The peak of $\partial I(x, y)/\partial x$ is typically observed at the particle edge corresponding to nearly the 11th pixel from the particle center. As shown in figure 4(*b*), particle A with well-defined outline has a steeper slope (dashed line) than that of particle B with blurred outline, which indicates that the slope of $\partial I(x, y)/\partial x$ curve provides a criterion for how well defined is the particle outline. Thus, we define the mean image-intensity gradient β as follows:

$$\beta = \frac{\left.\frac{\partial I(x,y)}{\partial x}\right|_{\max} - \left.\frac{\partial I(x,y)}{\partial x}\right|_{0.25D}}{0.25D}, \qquad (3)$$

where $\partial I(x, y)/\partial x|_{\max}$ is the maximum value of the 'image-intensity gradient' and $\partial I(x, y)\partial x|_{0.25D}$ is the value at the position $0.25D$ away from the grid at which the maximum value is observed. Actually, the intensity of particle B may be higher than that of particle A, while β_A is larger than β_B, indicating that the higher the value of β is, the better the outline of the particle is defined. Thus, we take β as a criterion for identifying a large particle, by including the particle image among the data set if β of that particle is greater than a certain reference β_{ref}. The constant 0.25 is only meaningful since it well describes the curve of the image-intensity gradient linearly. However, this value is not critical to estimating the relative differences of β among the test particles. We may

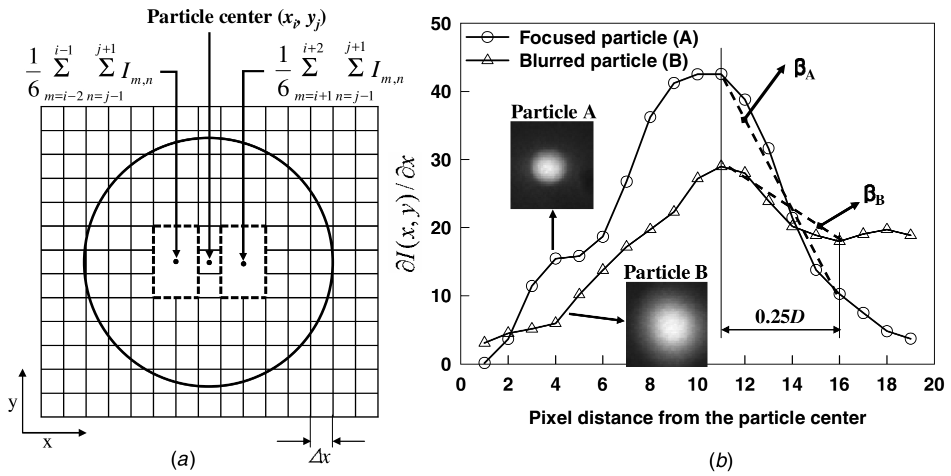

Figure 4. Calculation of mean image-intensity gradient β, where $D = 6\ \mu$m and $M = 40$. (*a*) Schematic of the test particle image where the center of the particle is at (x_i, y_j), and the grids represent pixel elements in a particle image frame. (*b*) Plots of 'image-intensity gradient' from equation (2) against pixel distance from the center of a focused particle (particle A) and an out-of-focus particle (particle B).

suggest that one can possibly take this constant in the range of 0.25–0.35.

2.8. Calibration of measurement depth

The measurement depth is the plane thickness of the particle image obtained in an optical microscope by the volume illumination method, which determines the spatial resolution in the depthwise direction; the smaller the measurement depth, the higher the resolution in depth [43]. However, if the resolution in depth is low, particle migration can be underestimated because unwanted particles may be observed near the centerline of the channel due to the poor resolution. Meinhart *et al* [43] theoretically derived the measurement depth as $\delta_{zm} = 3n\lambda_o/\mathrm{NA}^2 + 2.16D/\tan\theta + D$, which is twice the distance from the object plane to the location where the particle image is nearly unfocused. Thus, the particle image does not contribute to the velocity measurement, which occurs when its intensity drops off 10% of the maximum intensity of well-focused particle image, as validated by their experimental study [43].

Consequently, according to their theory, we expect that there are both blurred particle images and the particle images with well-defined outlines within the measurement depth, since the particle image whose intensity is less than 10% of that of the well-focused particle image may correspond to the burred particle. As mentioned earlier, we only deal with the particle images with well-defined outlines as our data. In what follows next, we propose a newly defined measurement depth, which is based on the value of β described in section 2.7 and supposedly gives better depth resolution than the particle image intensity as used in the previous study [43].

The calibration method for defining this newly defined measurement depth is depicted in figure 5(*a*), which utilizes 6 μm test particles confined in cured PDMS to make these particles immobile. Confinement of these test particles in cured PDMS was successfully achieved by the following two steps: (1) we placed a drop of particle suspension on a coverslip, (2) after the drop evaporated, a small amount of PDMS mixed with curing agent were cast onto the coverslip and cured in the atmosphere. Then, we obtained a series of particle images at discrete axial positions where a piezo-electric linear motor (PUML40, Piezo Technology, Korea) with sub-micron resolution replaces the fine focus knob of the microscope for scanning the object plane of the objective lens. Thus, β from the particle image at each axial position is calculated from equations (2) and (3) and represented against the axial positions according to the lens magnification and particle size, as shown in figure 5(*b*). Each curve shows nearly the Gaussian distribution with the maximum value of β at $z = 0$, and the width of the hump for one case ($M = 40$ and $D = 6\ \mu$m) is narrower than that of the other case ($M = 10$ and $D = 10\ \mu$m). As a threshold level, we take $\beta_{\mathrm{ref}} = 0.9$ and 0.81 for the cases of $M = 10$ and $M = 40$, respectively. For these values of β_{ref}, the measurement depth is about 7.24% of the channel height for $D_h = 140.9\ \mu$m and about 5.74% for $D_h = 87.5\ \mu$m, which implies that the measurement depth is so small that the observation is made on a nearly two-dimensional plane.

3. Results and discussions

Test particles of two different sizes were adopted to assess the particle size effect on the lateral migration when $\lambda \approx 14$ (see table 1). However, as will be discussed later (in figures 7, 9 and 10), we did not observe any significant particle size effect in the range of our investigation. We chose a specific particle size ratio of $\lambda \approx 14$ mainly because it is frequently encountered in the fundamental studies on lateral migration of particles [3, 10, 24] and in the flow phenomena in microfluidic devices handling blood cell or plasma separation [32, 34]. In other words, the diameter of a human red blood cell is about 7–8 μm, and that of a human white blood cell is about 9–20 μm, while in many lab-on-a-chip devices dealing with blood cell or plasma separation [32, 34] the dimensions of the microchannel is

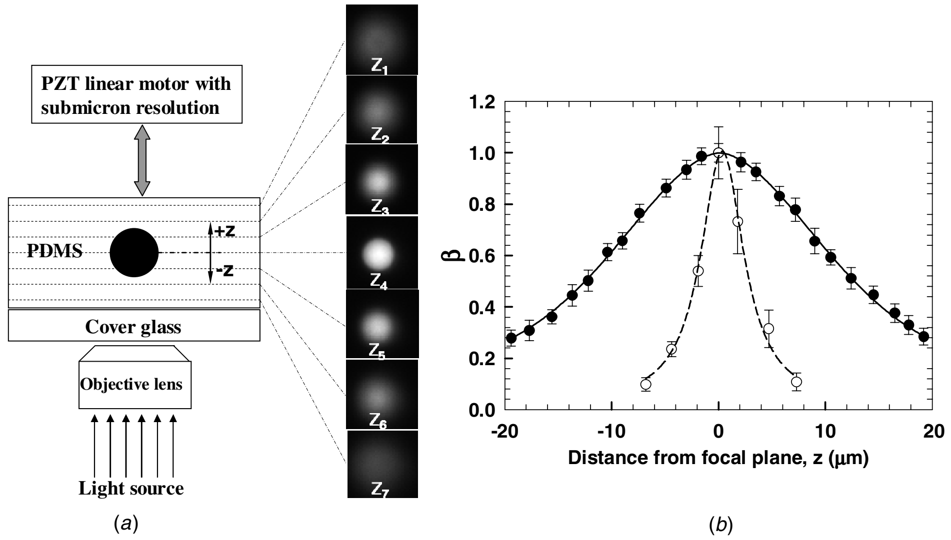

Figure 5. Calibration of the measurement depth, based on the criterion of mean image-intensity gradient β: (*a*) a schematic indicating calibration method (not to scale), (*b*) calibration results for two different objective lenses according to the particle size; (●) $M = 10$ and $D = 10$ μm; (○) $M = 40$ and $D = 6$ μm.

usually in the order of 100 μm. Therefore, it was considered that $\lambda \approx 14$ reasonably represents such assays. It is noted that in the present study we are interested in presenting our experimental results for numerous values of *Re*, which alone is quite laborious and requires a very careful analysis. A broader range of investigation of the particle size effect on the lateral migration remains to be the subject of a very interesting future work.

More importantly, once particle image frames are obtained, the identification of test particles is performed using the method described earlier, and the locations of the particles are determined by using the 2D Gaussian curve fitting of the particle image intensity with sub-pixel resolution, as adopted for the tracer particles.

3.1. Spatial distribution of particles over the channel width

In order to evaluate the lateral migration of the test particles, the probability density function (PDF) has been adopted to present their spatial distribution along lateral positions, which can be defined as follows:

$$f(y) = \frac{\sum_{k=1}^{k=400} N_k(y, y + \mathrm{d}y)}{\sum_{y=-H/2}^{y=H/2} \sum_{k=1}^{k=400} N_k(y, y + \mathrm{d}y)} \quad (4)$$

where $N_k(y, y + \mathrm{d}y)$ is the number of particles between the lateral positions y and $y + \mathrm{d}y$ in the kth image frame at a given experimental condition, $\sum_{y=-H/2}^{y=H/2} \sum_{k=1}^{k=400} N_k(y, y + \mathrm{d}y)$ is the total number of particles, summed over the channel width H and all the particle image frames. It is noticed that $f(y)$ is a PDF representing the fraction of the number of particles between y and $y + \mathrm{d}y$, such that $\int_{-H/2}^{H/2} f(y)\,\mathrm{d}y = 1$.

In figure 6, we present spatial distributions of the neutrally-buoyant particles over H at $Re = 2.43$, 9.01 and 18.37. At $Re = 2.43$, particle distribution is somewhat uniform across the channel cross section, so that particle migration is not typically observed at such a small *Re* [23]. However, as *Re* increases, particles drift away from the wall and away from the center of the channel, which originates from the wall lift near the wall and velocity gradient near the centerline [25, 29]. Consequently, particles accumulate at a certain equilibrium position where the peaks are observed, so that the number of particles around the center of the channel is clearly reduced. This phenomenon is analogous to what is observed in previous experiments for tube flows [3, 27].

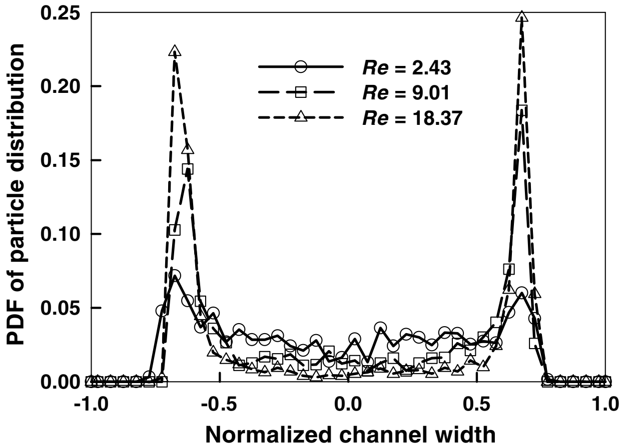

Figure 6. Spatial distributions of large test particles over normalized lateral positions at various *Re* for $D_h = 140.9$ μm.

The trend of the maximum PDF value is shown as a function of *Re* in figure 7 where the maximum PDF value increases as *Re* increases, which gives a good quantification of the particle migration rate in terms of *Re*. That the maximum PDF increases means that the particle migration more markedly occurs. However, according to a previous study [27] on Poiseuille flow through a tube of $D_t = 8$ mm,

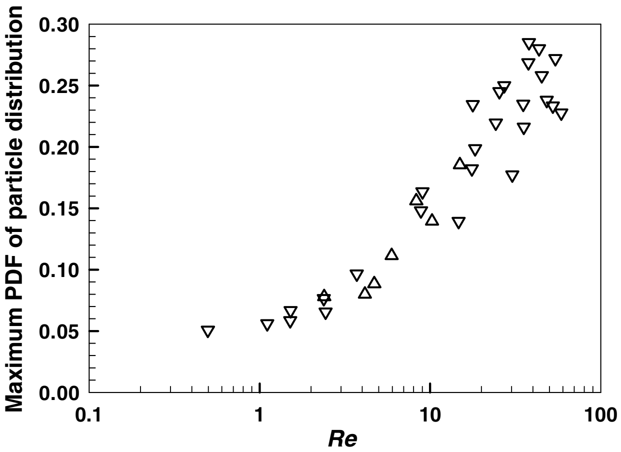

Figure 7. Maximum PDF values of the particle distribution against *Re*, representing the rate of lateral migration: (△) $D_h = 87.5\ \mu$m ($\lambda = 14.5$); (▽) $D_h = 140.9\ \mu$m ($\lambda = 14.1$). That the maximum PDF value is higher means that the particle migration occurs more prominently. However, significant difference between the maximum PDF for $D_h = 87.5\ \mu$m and that for $D_h = 140.9\ \mu$m hardly appears. This is because the ratio of the particle size to the channel size is nearly identical [20].

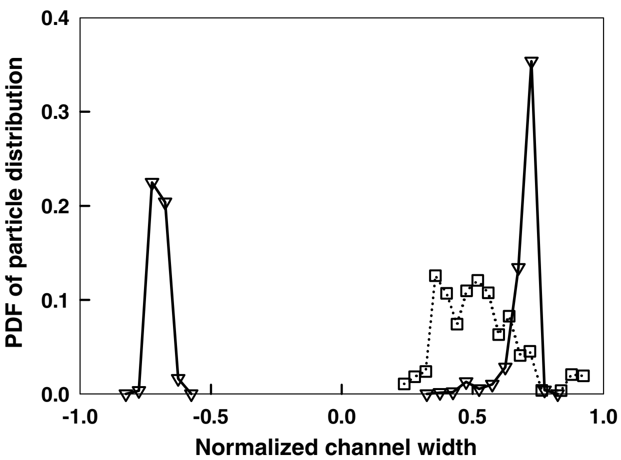

Figure 8. Spatial distribution of the test particles: (▽) present study ($\dot{\gamma}_w \approx 2.5 \times 10^4 s^{-1}$, $Re = 37.91$, $\lambda \approx 14$); (□) results of Matas *et al* in a circular tube of 8 mm diameter [27] ($\dot{\gamma}_w = 2.8 \times 10^2 s^{-1}$, $Re = 1650$, $\lambda = 17$).

the maximum PDF value decreases at relatively large *Re*, since there exist multiple-equilibrium positions, which gives rise to a spreading of particle distribution rather than a sharp peak. On the other hand, it is observed in the present study that the particles definitely migrate toward the equilibrium position at $Re \approx 37$ (also see figure 8), which indicates that inertial migration is fully developed at this *Re*. Similarly, a numerical simulation study [31] confirms that this phenomenon has also been observed at *Re* = 100 in a square duct for a larger particle size of $\lambda = 9$.

Since we can hardly obtain any existing experimental data that provide spatial distributions of particles in a square microchannel, we only compare our results with that of Matas *et al* [27] in a tube flow with $D_t = 8$ mm at $\lambda = 17$, as shown in figure 8. We first consider the entry length of inertial migration defined by $L_e/D_t = 6\pi A^{-1} Re^{-1}(D_t/D)^3$, which is predicted by matched asymptotic theory [26, 28], where L_e is the entry length and A is the magnitude of the scaled force in their theory. According to this theory, the entry length $L_e/D_t = 310$ at *Re* = 1500 and $\lambda = 17$, which means that particle distribution measured by Matas *et al* in figure 8, has been obtained in the fully-developed region, because the measurement was made at $L/D_t = 310$ and $Re = 1650$. A typical feature of particle distribution when measured in the fully-developed region is that there are no particles near the center of the channel. In this regard, it is considered that our results in figure 8 are obtained for a nearly fully-developed flow region at substantially smaller Reynolds number of $Re \approx 37$. Thus, it can be argued that the depletion of particles around the center of the channel is observed at a much smaller *Re* in the present study than that of Matas *et al*.

It might be explained that the large *Re* difference is offset by the effect of the particle size ratio (λ) and the measurement distance (L/D_h) from the inlet. In other words, if λ is small and L/D_h is large, particle migration can be observed at small *Re*. λ and L/D_h in the present study are about 14 and 400, respectively, while those of Matas *et al* in figure 8 are 17 and 310, respectively. In this regard, it might serve as an explanation for the depletion of particles that we have reached fully-developed particle distribution already at smaller *Re*. However, this explanation is less persuasive because, according to the theory, $L_e/D_t = 430$ at *Re* = 500 and $\lambda = 15$, as calculated by Matas *et al*, while we obtained our data at $L/D_h = 400$, $Re \approx 37$ and $\lambda = 14.1$. Namely, if we exclude the particle size effect (incidentally, in the theory $\lambda = 15$ and in our experiment $\lambda \approx 14$), the particle distribution of the present result should not necessarily reflect the feature of the fully-developed flow region, because, according to the asymptotic theory [27], our experimental condition ($L/D_h < 430$, $Re \ll 500$) is believed to be in the transient region. Thus, other factor should be taken into consideration for more comprehensible explanation.

As for another possible explanation for the occurrence of the particle migration at such a small *Re*, we consider the particle Reynolds number $Re_p = U_{\max}(0.5D)^2/\nu H$ adopted by Feng *et al* [29]. This can be rearranged in terms of the shear rate ($\dot{\gamma}_w = 4U_{\max}/H$) such as $Re_p = \dot{\gamma}_w D^2/16\nu$ and as similarly defined in the form of $Re_p = \dot{\gamma}_w D^2/\nu$ in the numerical simulation [44]. As Re_p increases, a particle migrates fast to its equilibrium position. For instance, a particle reaches its equilibrium position four times faster when the shear rate increases five times as discussed in Feng *et al* [29]. The shear rate ($\dot{\gamma}_w \approx 4.4U_{\max}/D_h$) of the present study at $Re \approx 37$, based on the approximation given by Purday [41] in figure 8, is approximately 2.5×10^4 s^{-1} and that ($\dot{\gamma}_w = 4U_{\max}/D_t$) of Matas *et al* is 2.84×10^2 s^{-1}, so that there is a big difference in the shear rates. Thus, we consider that the particles subject to a high shear rate migrate even at small *Re*, which can be induced due to the scale effect in such a microscale flow. Moreover, according to the simulation results for neutrally-buoyant particles in 3D tube flow [35], pressure (p) distribution on a particle surface as a driving force of lateral

Table 3. Summary of possible errors in determining the particle equilibrium position and outermost edge: (a) the error ϵ_r which is the pixel reading error in determining channel walls in the image frame, (b) the error ϵ_s related to the spatial resolution of dy in equation (4) when calculating PDF, and (c) the error ϵ_p due to mislocation of particle center in the 2D Gaussian curve fitting.

Errors	$\lambda = 14.5$	$\lambda = 14.1$
ϵ_r (μm)	0.64	1.28
ϵ_s (μm)	0.88	1.44
ϵ_p (μm)	0.30	0.50
$\sum \epsilon_{\text{total}}$ (μm)	1.82	3.22
$\sum \epsilon_{\text{total}}/D_h \times 100$ (%)	2.08	2.28

migration is proportional to $\dot{\gamma}^2$, where $\dot{\gamma}$ is the local shear rate: a stronger shear flow creates a stronger migration force. On the other hand, it is noticed that there is no significant difference between the maximum PDFs for the smaller channel (D_h = 87.5 μm) and that for the larger channel (D_h = 140.9 μm), as shown in figure 7. In fact, the shear rate in the smaller channel is only about 2.5 times higher than that of the larger channel. We therefore consider that this minor difference in the shear rate cannot induce a striking contrast between the maximum PDFs.

3.2. Equilibrium position

The particle equilibrium position y_e, which is defined as the lateral distance from the centerline of the channel to the peak position of the particle concentration distribution, is found to be one of the most interesting observations in microscale flows. However, it has been insufficiently reported in microscale flows, while it is still very important in view of its application to microfluidics, such as those for cell concentration and separation. Biological particles can be concentrated better in capillary-based microfluidic devices by using design which shifts y_e toward the wall while keeping the particle distribution curve sharp [5, 6].

To aid better understanding of how y_e can be defined in the present study, we consider the particle distribution at Re = 18.37 as shown in figure 6, where the peaks are typically observed. To obtain y_e, rather than to choose y_e from either of the lateral positions of the peaks, it is reasonable that the distances between the two peaks are averaged because the lateral distance from the centerline to each peak may not be necessarily identical for the cases of the experimental studies, as discussed in [10, 27]. Meanwhile, there are possible experimental errors in determining y_e, as shown in table 3: the pixel reading error ϵ_r, error ϵ_s associated with dy when calculating PDF and error ϵ_p due to the particle mislocation in the 2D Gaussian fitting. It is proved that ϵ_p is less than 5% of the particle diameter. Accordingly, overall errors $\left(\sum \epsilon_{\text{total}} = \epsilon_r + \epsilon_s + \epsilon_p\right)$ and percent errors according to the channel size $\left(\sum \epsilon_{\text{total}}/D_h \times 100\%\right)$ are summarized in table 3 for each particle size. Figure 9 shows y_e as a function of Re. There is a plateau in equilibrium position at small Re in the range of $Re \leqslant 20$. As Re further increases, however, equilibrium position increases as well, which originates from the imbalance of inward and outward force components [27, 28]. Meanwhile, there is no significant difference of equilibrium positions between the cases of D_h = 87.5 μm and D_h = 140.9 μm. This is because the ratio of the particle size to the channel size is nearly identical [20]. Moreover, it is of great interest that we found the critical Re in the range of $20 \leqslant Re \leqslant 30$, at which y_e begins to increase.

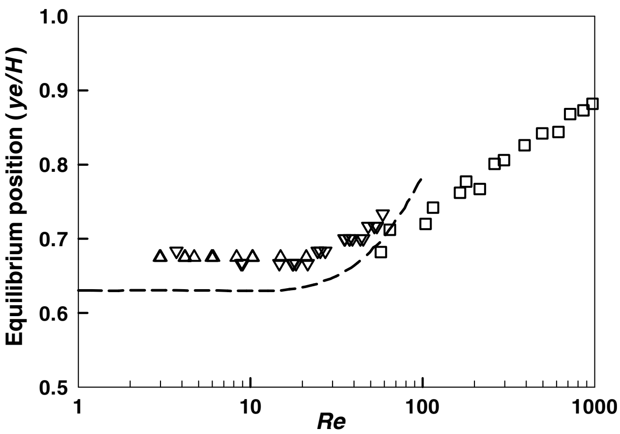

Figure 9. Particle equilibrium position as a function of Re: (△ and ▽) present study at $\lambda = 14.5$ and $\lambda = 14.1$, respectively; (□) Matas *et al* [27] for circular Poiseuille flow at $\lambda = 15$; (- - - -) asymptotic theory by Schonberg and Hinch [26] for plane Poiseuille flow.

Schonberg and Hinch [26], who constructed a correlation between y_e and this critical Re, numerically showed the trend curve of the equilibrium position of a neutrally-buoyant particle in plane Poiseuille flow by using matched asymptotic theory for Reynolds number less than approximately 100. From their theory, the critical Re has been estimated in the range of $20 \leqslant Re \leqslant 30$, where the Reynolds number based on the maximum fluid velocity in their theory was recalculated with the mean fluid velocity for the comparison. Moreover, from direct numerical simulation (DNS) results for 3D Poiseuille flow, Zhu [35] showed that the critical Re is 25, where actually the critical Re is 50 in his work because he defined Re based on $U_{\max}$ rather than U. The critical Re estimated in the present experiment is in very good agreement with that predicted by Schonberg and Hinch [26] and by Zhu [35]. As for the numerical values of particle equilibrium positions, there is a disagreement with the theory. That is, y_e in the square channel flow is closer to the wall than that of the planar channel flow [31]. This discrepancy is possibly due to the corner effect in a square channel. We propose that further study including numerical simulation is needed to better explain this discrepancy.

3.3. Outermost edge of the particle cluster

Now, we discuss the outermost edge of particle cluster y_o, which was introduced by Segré and Silberberg [3], and its applications regarding microfluidics. The outermost edge can be defined by the lateral distance from the centerline of the channel to the farthest edge of the particle cluster. In order to determine y_o, lateral distances from the centerline to the two edges shown on the PDF distribution are averaged for the same

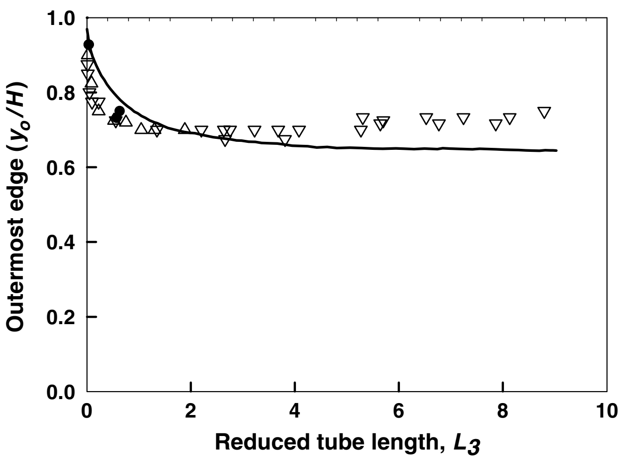

Figure 10. Outermost edge of the particle cluster as a function of the reduced tube length L_3 [3]: (△) present study ($\lambda = 14.5$, $D_h = 87.5\ \mu$m); (▽) present study ($\lambda = 14.1$, $D_h = 140.9\ \mu$m); (•) Segré and Silberberg [3] ($\lambda \approx 14$); (——) quadratic force model [3].

reason as considered in determining y_e. Experimental errors in measuring y_o are also coincident with those in measuring y_e, as shown in table 3. We consider the reduced tube length [3] defined by

$$L_3 = \frac{\rho U L}{\mu}\left(\frac{D}{D_t}\right)^3 \quad \text{or} \quad Re\left(\frac{L}{D_t}\right)\left(\frac{D}{D_t}\right)^3 \tag{5}$$

where D_t is replaced by D_h in the present study.

In figure 10, the outermost edge obtained in the present study is compared with available data obtained by Segré and Silberberg [3]. For $L_3 \leqslant 3$, y_o exponentially decreases, as L_3 increases. However, as L_3 further increases, y_o slightly increases for the case of $D_h = 140.9\ \mu$m. For small L_3, the quadratic force model proposed by Segré and Silberberg [3] overestimates our experiments, since the theory involves the restriction of finite particle dimension at the tube wall. However, for large L_3, the theory underestimates our experimental data due to the high Re effect [3]: as Re increases, y_e is shifted to the wall, which causes y_o to also move closer to the wall.

We consider the particle-free layer thickness $H - y_o$ corresponding to the layer of volume of the particle-free region in suspension flows. In microfluidic devices where plasma is separated from the whole blood, the main technique is to extract plasma from the volume of the particle-free region [32–34]. It is expected that the best performance can be achieved by making the particle-free layer thickness as enlarged as possible for the higher plasma selectivity with a large amount of plasma. In figure 10, the particle-free layer thickness decreases as L_3 increases for $L_3 \geqslant 3$, which gives an adverse effect on the performance. In fact, the decrease of the particle-free layer thickness for $L_3 \geqslant 3$ is due to the high Re effect [3], so that it is preferred to control L_3 by keeping Re as small as possible. In contrast, regarding the applications to concentration of bio particles [5, 6], it is necessary to decrease the outermost edge. In other words, the particle-free layer thickness should be increased. Thus, controlling the particle-free-layer thickness under lateral migration should be considered in accordance with the applications being considered.

3.4. Extended discussion

We have treated neutrally-buoyant particles so far, while practical applications involve slightly non-neutrally-buoyant particles or cells in microchannels (i.e., biological particles or blood cells suspended in saline solution [5, 32–34] or plasma of blood [32, 33], respectively). However, the results obtained in this study still hold for such applications, since the pattern of lateral migration for such slightly non-neutrally-buoyant particles is similar to that of neutrally-buoyant particles [27]. Besides, although biological particles are rarely spherical, non-spherical particles exhibit similar behavior to that observed in spherical particles, as reported for discs and rods by Cox and Mason [20] as well as for red blood cells by Uijttewaal *et al* [10]. Hence, it can be argued that the results obtained from the present study do hold for the practical applications in microchannel flows.

4. Conclusion

An experimental study has been carried out to investigate the lateral migration of neutrally-buoyant particles in microscale flows through square microchannels in the range of Reynolds numbers of $0.06 \leqslant Re \leqslant 58.65$. An epi-fluorescent microscope, a double-pulsed Nd:YAG laser and a cooled-CCD camera are utilized. Fluorescent-labeled polymer microspheres with different sizes (small tracer particles and large test particles) are used. Flow Reynolds numbers are obtained from tracer particles using the particle-tracking algorithm. Novel imaging techniques for identifying the test particles and defining the measurement depths of these particles have been proposed. The spatial distribution of spherical particles under lateral migration is presented with respect to Re. Lateral migration markedly occurs at substantially small Re, since high shear rate is induced due to the scale effect. The particle equilibrium position is obtained as a function of Re, and more specifically, critical Re where the equilibrium position starts to increase is shown to exist in the range of $20 < Re < 30$, which is in very good agreement with that estimated by previous numerical simulations ($Re \sim 25$) for circular Poiseuille flow and planar Poiseuille flow. The outermost edge is in good agreement with the previous experiments, which gives good quantifications for designing of microfluidic devices.

Acknowledgments

This work was supported by grant no. R01-2005-000-10558-0 from the Basic Research Program of the Korea Science & Engineering Foundation (KOSEF) and also in part by the Micro Thermal System Research Center at SNU, under the auspices of KOSEF.

References

[1] Stone H A and Kim S 2001 Microfluidics: basic issues, applications, and challenges *AIChE J.* **47** 1250–4

[2] Gravesen P, Branebjerg J and Jensen O S 1993 Microfluidics—a review *J. Micromech. Microeng.* **3** 168–82

[3] Segré G and Silberberg A 1962 Behaviour of macroscopic rigid spheres in Poiseuille flow: Part 2. Experimental results and interpretation *J. Fluid Mech.* **14** 136–57

[4] Karnis A, Goldsmith H and Mason S G 1966 The flow of suspensions through tubes: Part 5. Inertial effects *Can. J. Chem. Eng.* **44** 181–93

[5] Wickramasinghe S R, Lin W C and Dany D S 2001 Separation of different sized particles by inertial migration *Biotechnol. Lett.* **23** 1417–22

[6] Rakow A L and Fernald D 1991 Concentration of *spirulina* suspensions by radial migration with flow through vertical tees *Biotechnol. Prog.* **7** 343–7

[7] Zheng J and Yeung E S 2003 Counting single DNA molecules in a capillary with radial focusing *Aust. J. Chem.* **56** 149–53

[8] Poiseuille J L M 1836 Recherches sur les causes du mouvement du sang dans les Vaisseaux Capillaires *Ann. Sci. Nat.* **5** 111–5

[9] Fahræus R and Lindqvist T 1931 The viscosity of the blood in narrow capillary tubes *Am. J. Physiol.* **96** 562–8

[10] Uijttewaal W S J, Nijhof E J and Heethaar R M 1994 Lateral migration of blood cells and microspheres in two-dimensional Poiseuille flow: a laser-Doppler study *J. Biomech.* **27** 35–42

[11] Eloot S, Bisschop F D and Verdonck P 2004 Experimental evaluation of the migration of spherical particles in tree-dimensional Poiseuille flow *Phys. Fluids* **16** 2282–93

[12] Xuan X and Li D 2006 Particle motions in low-Reynolds number pressure-driven flows through converging-diverging microchannels *J. Micromech. Microeng.* **16** 62–9

[13] Staben M E and Davis R H 2005 Particle transport in Poiseuille flow in narrow channels *Int. J. Multiphase Flow* **31** 529–47

[14] Staben M E, Zinchenko A Z and Davis R H 2003 Motion of a particle between two parallel plane walls in low-Reynolds-number Poiseuille flow *Phys. Fluids* **15** 1711–33

[15] Hsieh S S, Lin C Y, Huang C F and Tsai H H 2004 Liquid flow in a micro-channel *J. Micromech. Microeng.* **14** 436–45

[16] Koo J and Kleinstreuer C 2003 Liquid flow in microchannels: experimental observations and computational analyses of microfluidics effects *J. Micromech. Microeng.* **13** 568–79

[17] Peng X F, Peterson G P and Wang B X 1994 Friction flow characteristics of water flowing through rectangular microchannels *Exp. Heat Transfer* **7** 249–64

[18] Sharp K V 2001 Experimental investigation of liquid and particle-laden flows in microtubes *PhD Dissertation* University of Illinois at Urbana–Champaign

[19] Oliver D R 1962 Influence of particle rotation on radial migration in the Poiseuille flow of suspensions *Nature* **194** 1269–71

[20] Cox R G and Mason S G 1971 Suspended particles in fluid flow through tubes *Ann. Rev. Fluid Mech.* **3** 291–316

[21] Repetti R V and Leonard E F 1964 Segré–Silberberg annulus formation: a possible explanation *Nature* **203** 1346–8

[22] Halow J S and Wills G B 1970 Radial migration of spherical particles in Couette systems *AIChE J.* **16** 281–6

[23] Goldsmith H L and Mason S G 1962 The flow of suspensions through tubes: I. Single spheres, rods, and discs *J. Colloid Sci.* **17** 448–76

[24] Jeffrey R C and Pearson J R A 1965 Particle motion in laminar vertical tube flow *J. Fluid Mech.* **22** 721–35

[25] Ho B P and Leal L G 1974 Inertial migration of rigid spheres in two-dimensional unidirectional flows *J. Fluid Mech.* **65** 365–400

[26] Schonberg J A and Hinch E J 1989 Inertial migration of a sphere in Poiseuille flow *J. Fluid Mech.* **203** 517–24

[27] Matas J P, Morris J F and É Gauzzelli 2004 Inertial migration of rigid spherical particles in Poiseuille flow *J. Fluid Mech.* **515** 171–95

[28] Asmolov E S 1999 The inertial lift on a spherical particle in a plane Poiseuille flow at large channel Reynolds number *J. Fluid Mech.* **381** 63–87

[29] Feng J, Hu H H and Joseph D D 1994 Direct simulation of initial value problems for the motion of solid bodies in a Newtonian fluid: Part 2. Couette and Poiseuille flows *J. Fluid Mech.* **277** 271–301

[30] Cho S H, Choi H G and Yoo J Y 2005 Direct numerical simulation of fluid flow laden with many particles *Int. J. Multiphase Flow* **31** 435–51

[31] Chun B and Ladd A J C 2006 Inertial migration of neutrally buoyant particles in a square duct: an investigation of multiple equilibrium positions *Phys. Fluids* **18** 031704

[32] Jäggi R D, Sandoz R and Effenhauser C S 2007 Microfluidic depletion of red blood cells from whole blood in high-aspect-ratio microchannels *Microfluid Nanofluid* **3** 47–53

[33] Yang S, Ündar A and Zahn J D 2006 A microfluidic device for continuous, real time blood plasma separation *Lab Chip* **6** 871–80

[34] VanDelinder V and Groisman A 2006 Separation of plasma from whole human blood in a continuous cross-flow in a molded microfluidic device *Anal. Chem.* **78** 3765–71

[35] Zhu M 2000 Direct numerical simulation of solid–liquid flow of Newtonian and viscoelastic fluids *PhD Dissertation* University of Pennsylvania

[36] Meinhart C D, Wereley S T and Santiago J G 1999 PIV measurements of a microchannel flow *Exp. Fluids* **27** 414–9

[37] Happel J and Brenner H 1983 *Low Reynolds Number Hydrodynamics. With Special Applications to Particulate Flow* (Leyden, The Netherlands: Noordhoff)

[38] Xia Y and Whitesides G M 1998 Soft lithography *Annu. Rev. Mater. Sci.* **28** 153–84

[39] Yan D, Yang C, Nguyen N-T and Huang X 2007 Diagnosis of transient electrokinetic flow in microfluidic channels *Phys. Fluids* **19** 017114–10

[40] Jin S, Huang P, Park J, Yoo J Y and Breuer K S 2004 Near-surface velocimetry using evanescent wave illumination *Exp. Fluids* **37** 825–33

[41] Purday H F P 1949 *An Introduction to the Mechanics of Viscous Flow* (New York: Dover)

[42] Olsen M G and Adrian R J 2000 Out-of-focus effects on particle image visibility and correlation in microscopic particle image velocimetry *Exp. Fluids* **29** s166–74

[43] Meinhart C D, Wereley S T and Gray M H B 2000 Volume illumination for two-dimensional particle image velocimetry *Meas. Sci. Technol.* **11** 809–14

[44] Joseph D D and Ocando D 2002 Slip velocity and lift *J. Fluid Mech.* **454** 263–86